Supplementary Information

Tough asymmetric thermochromic ionogels via dynamic in situ phase separation for passive/active smart optical switching

Guoli Du,[1] Jianing Li,[1] Changxing Wang,[1] Jianing Li,[1] Yayun Ning,[1] Yifan Yue,[1] Yuechi Xie,[1] Sen Yang,[1]* Xuegang Lu[1]*

[1]School of Physics, MOE Key Laboratory for Nonequilibrium Synthesis and Modulation of Condensed Matter, Xi'an Jiaotong University, Xi'an 710049, China

*Corresponding author: xglu@mail.xjtu.edu.cn; yangsen@mail.xjtu.edu.cn

This file includes

Supplementary Methods

Materials

The monomers n-butyl acrylate (BA) and N-isopropylacrylamide (NIPAM), Irgacure 1173, cross-linker ethylene glycol dimethacrylate (EGDMA) and N,N′-methylenebis(acrylamide) (MBAA), thermal initiator ammonium persulfate (APS), and accelerator N,N,N′,N′-tetramethylethylenediamine (TEMED) were purchased from Aladdin. The ionic liquid [Emim][TFSI] was purchased from Lanzhou Institute of Chemical Physics. The reagents used in the experiments were used as received without further purification, and the DI water used was purified by Master-Q30. Flexible graphene heating sheet with polyethylene terephthalate (PET) substrate and copper tape purchased from Shenzhen Nuanfeng Technology Co. The following materials were purchased from Alibaba: transparent sheets including glass, polymethyl methacrylate (PMMA), polyvinyl chloride (PVC), polycarbonate (PC); commercial tape including polyimide (PI), 3M VHB tape, 3M 9080 tape; and insulated foam boxes.

Preparation of pure PBA ionogels, bilayer ionogels and PNIPAM hydrogels

Pure PBA ionogels were prepared in a similar manner as ATI-B in asymmetric ionogels, except that there was no subsequent in situ light curing. Physical bilayer ionogels were prepared by preparing ionogels with ATI-B and ATI-BN as precursors, respectively, and using an external force to adhere them together and overnight.

9.2 mmol of NIPAM was dissolved in 13 mL of DI water. Sequentially, 0.26 mmol of MBAA, 0.09 mmol of APS and 0.27 mmol of TEMED were added to the solution. The

solution was stirred at 0°C for 2 h and then placed in a refrigerator at 2-4°C overnight. The resulting gel was immersed in DI water for 48 h to obtain PNIPAM hydrogel.

Computational methods

Molecular dynamics (MD) simulations were performed within Materials Studio using the Forcite module. The initial computational model comprised a simulation box measuring 3.29 nm^3, containing 10 PBA chains (each with a polymerization degree of 10) and 22 [EMIM][TFSI] ionic liquid molecules. An initial amorphous structure was generated by subjecting this model to geometry relaxation using the COMPASS II force field. Subsequently, MD simulations employing the COMPASS II force field were carried out. The system underwent NPT ensemble equilibration for 100 ps using a Nosé thermostat and barostat to achieve system equilibration. For the analysis of structural and diffusional properties, NVT ensemble simulations were conducted for 1000 ps at temperatures of either 298K or 313K, employing a time step of 1.0 fs. Interaction energies were performed using the Dmol[3] code in Materials Studio software. Van der Waals correction of Grimme's DFT-D3 model[1] was used, together with the GGA/PBE[2, 3] exchange-correlation functional and a DNP basis set. Next, an energy convergence criterion of 1×10^{-5} Ha and a force convergence criterion of 0.002 Ha $Å^{-1}$ were set in the calculation. The interaction energy (E) was calculated by the following equation:

$$E = E_{A+B} - (E_A + E_B) \quad (1)$$

where E_A, E_B, and E_{A+B} are the energy of the isolate A, B, and A-B complex, respectively.

Mechanical performance test

Tensile and compression tests were performed using an electronic universal testing machine (3367, Instron, USA). The tensile samples were dumbbell-shaped with a tensile area size of 20×35×2 mm and a tensile speed of 50 mm min^{-1}. Sandpaper and tape were used to secure the ionogel to the fixture during testing. The compression specimen was cylindrical with a diameter of 10 mm and a height of 5 mm, and the compression speed was 50 mm min^{-1}; the maximum strain value for the compression cycle test was set at 70%. For the lap-shear experiments, two Al sheet were used as substrate sand glue was used to bond the ionogels to them. The contact area between the ionic gel and the aluminum sheet was 25×25 mm, and the test speed was 20 mm min-1. To demonstrate the excellent interfacial strength of the ATIs, two commercial double-sided adhesives (VHB and 9080) were purchased from 3M for comparison. For adhesion testing, ATIs were cut into 20×100×2 mm blocks. They were adhered to different substrates and to avoid air bubbles at the interface, pressed using a heavy weight and left overnight. PI tapes were used as a backing to avoid stretching of the ATIs during the tests. To test impact resistance, equal sized ATIs were sandwiched between two white PVC sheets, along with tempered glass, and a 1.25t vehicle was driven over them to assess their morphological integrity.

Surface hydrophobicity test

Surface hydrophobicity tests were performed on glass, PNIPAM hydrogel, and ATI using an optical contact angle meter (DSA100S, Kruss, Germany). The glass was ultrasonically cleaned and dried using DI water and alcohol prior to testing. Dust-free

paper was used to vacuum the water from the surface of the PNIPAM hydrogel. No additional treatment was performed on the ATI except for the use of alcohol to clean the surface of floating dust. ATIs were tested for surface droplet adhesion and antifouling ability using a mixture of toluidine blue and toner configured respectively. According to the Hamaker theory and the Young-Dupré equation[4, 5], the work of adhesion is given by the following equation:

$$W_{LS} = \gamma_L (1+\cos\theta) \quad (2)$$

where W_{LS} is the work of adhesion at the interface of the two phases, L and S represent liquids and solids, respectively; the surface tension (γ) of water at room temperature is 72 mN m^{-1}; and θ is the contact angle.

Smart cooling window test

Transmittance variations of ATIs in the 200-2500 nm wavelength range over 20-45°C were measured using a near-infrared spectrometer (NIRQUEST+2.5, Ocean Optics, USA) and a temperature-controlled accessory. To evaluate the cooling performance of the material, commercial foam boxes (inside diameter: 22.8×12×14.7 cm, wall thickness: 3 cm) with a top opening size of 12×12 cm were used as a model house with one window. Tempered glass, ATI (attached to glass, ATI-B side close to the glass), and air (open system) were used as the windows of the model house, respectively. A xenon lamp was used to simulate sunlight to evaluate the cooling ability of the material and a thermocouple (TA612C, TASI, China) was used for temperature monitoring. When the field test of smart cooling windows was conducted, a model house with different materials as windows was placed outdoors (Xi'an, China, May 20, 2025) and

the temperature inside was monitored for 24 h. To prepare the aesthetic smart windows, the shape of the ATI was customized using the template cutting method and stained using dyes.

Smart projection screen test

For localized opacity display of ATIs, a patterned customized flexible graphene heating sheet was used as a Joule heating substrate, which was powered using a DC power supply (24 V). To realize an in situ global opaque display of the ATI, the ATI body can be used as a flexible Joule heater. A signal generator (FY6900, Feiyi, China) and a high voltage amplifier (ATA-2041, Aigtek, China) were used to power the ATI. The local maximum temperature of the ATI can reach 50°C when the operating frequency and voltage were 10 kHz and 180 V, respectively. Electrochemical impedance spectra (EIS) of ATIs were obtained by an electrochemical workstation (PARSTAT MS, Princeton, USA), thermoregulated using a temperature control accessory, and temperature monitored using a thermocouple. The ionic conductivity of ATI was calculated by the following equation:

$$\sigma = \frac{L}{R_b \times S} \tag{3}$$

where σ is the ionic conductivity; L is the thickness of the specimen sandwiched between the electrodes; R_b is the intrinsic resistance of the specimen; and S is the contact area between the specimen and the electrode.

An infrared thermal imager (TiS55+, Fluke, USA) was used to visualize the local heat distribution on the ATIs. When used as smart projection screens, ATIs are transformed

opaque by indirect localized heating or direct Joule heating, and projections are made on their surfaces using a commercial micro-projector.

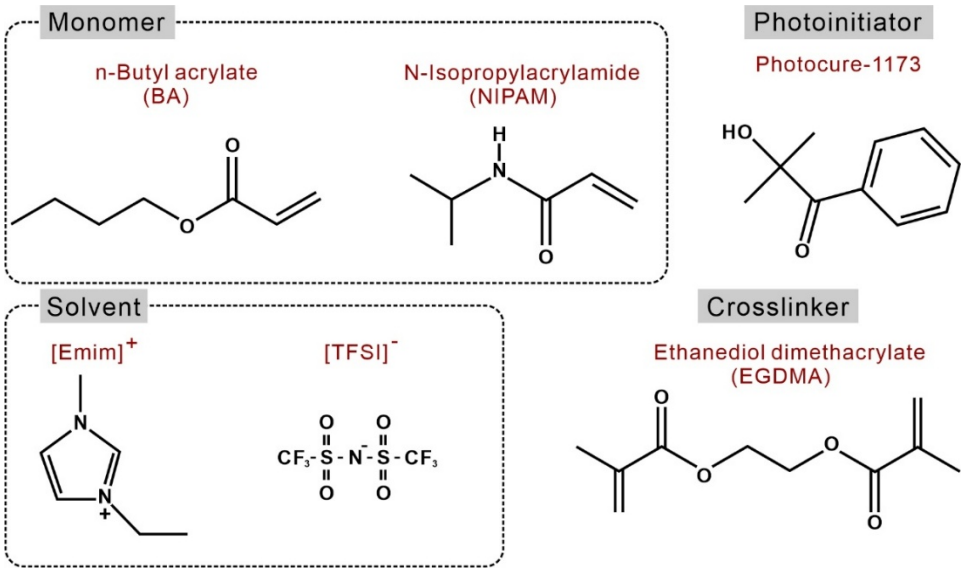

112

113 **Supplementary Figure 1. Molecular structures of chemicals used in the synthesis**

114 **of ATI precursors.**

115

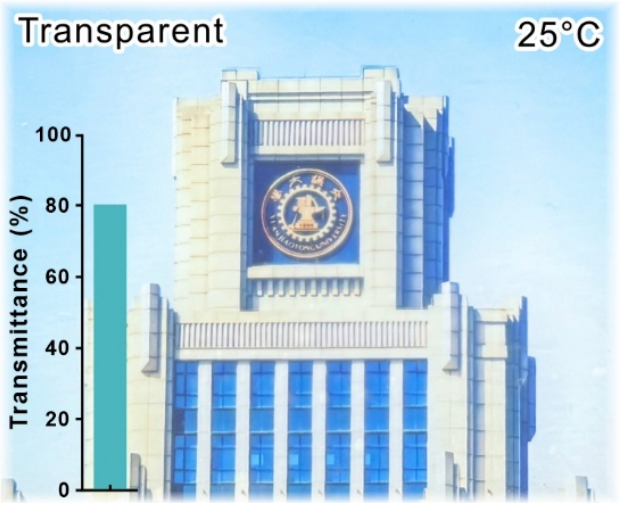

Supplementary Figure 2. Optical photograph of ATI at 25°C (Hanying building of XJTU in the background, used with permission), inset shows the transmittance of light at 550 nm wavelength.

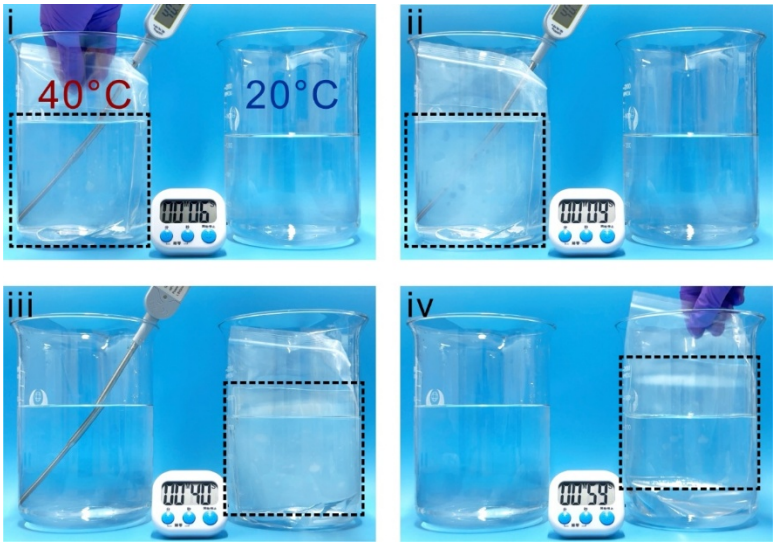

Supplementary Figure 3. The thermochromic process of ATI. Including i) immersion in hot water at 40°C; ii) an opaque transformation; iii) transfer to cool water at 20°C; and iv) return to a transparent state.

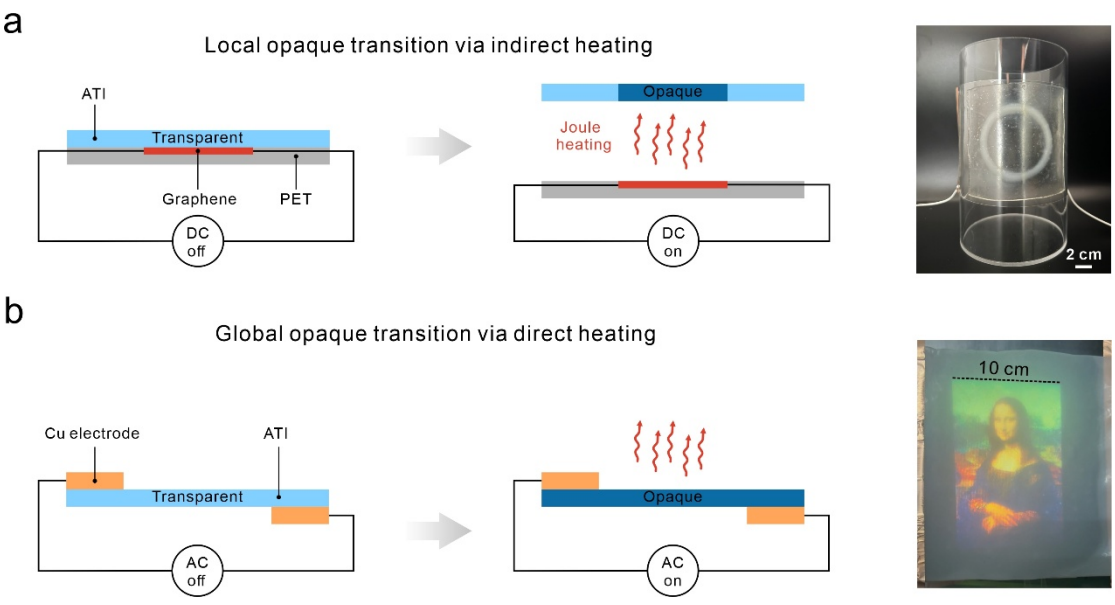

126

127 **Supplementary Figure 4. Local/global opaque transitions achieved by**
128 **indirect/direct Joule heating of ATI.** a) Schematic of the process of indirect Joule
129 heating of ATI using flexible graphene heating sheets (left) and local display effect
130 (right). b) Schematic of the process of direct Joule heating of ATI using alternating
131 current (left) and display effect of global projection screen (right).

132

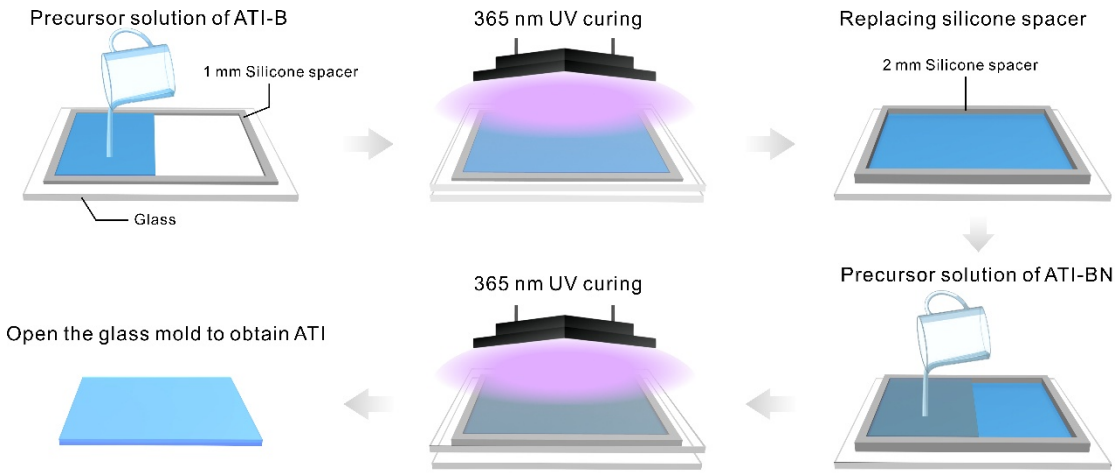

133

134 **Supplementary Figure 5. Schematic of the ATI preparation process.**

135

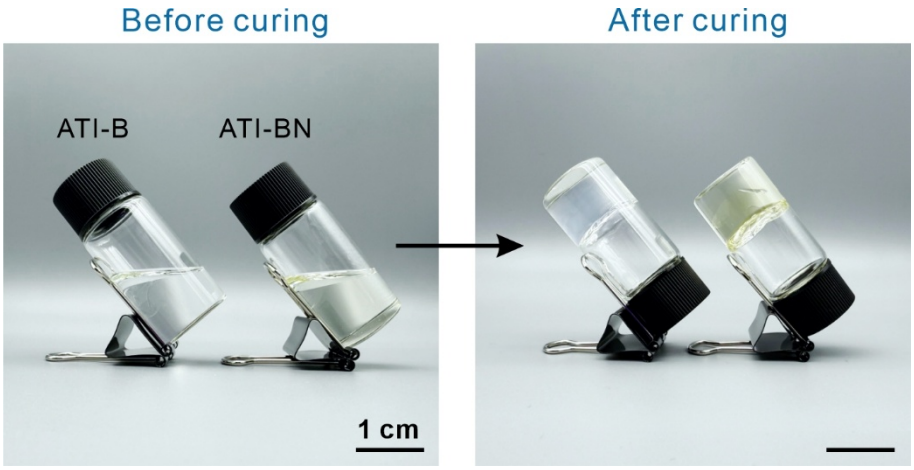

Supplementary Figure 6. Photographs of precursor solutions of ATI-B and ATI-BN before and after curing, respectively.

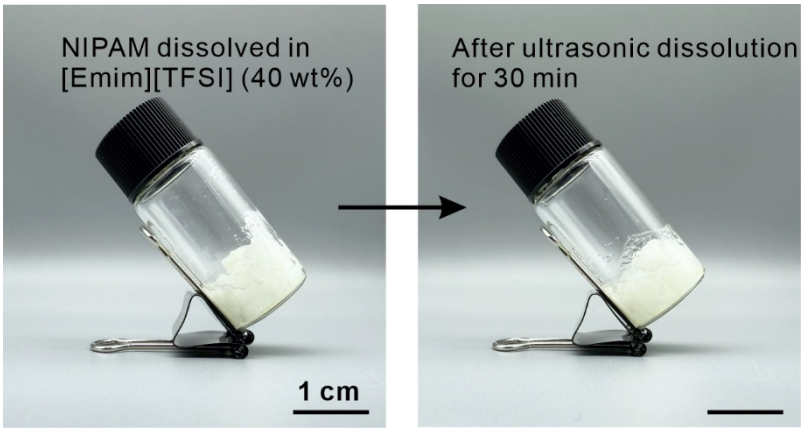

Supplementary Figure 7. Demonstration of NIPAM solubility in [Emim][TFSI].

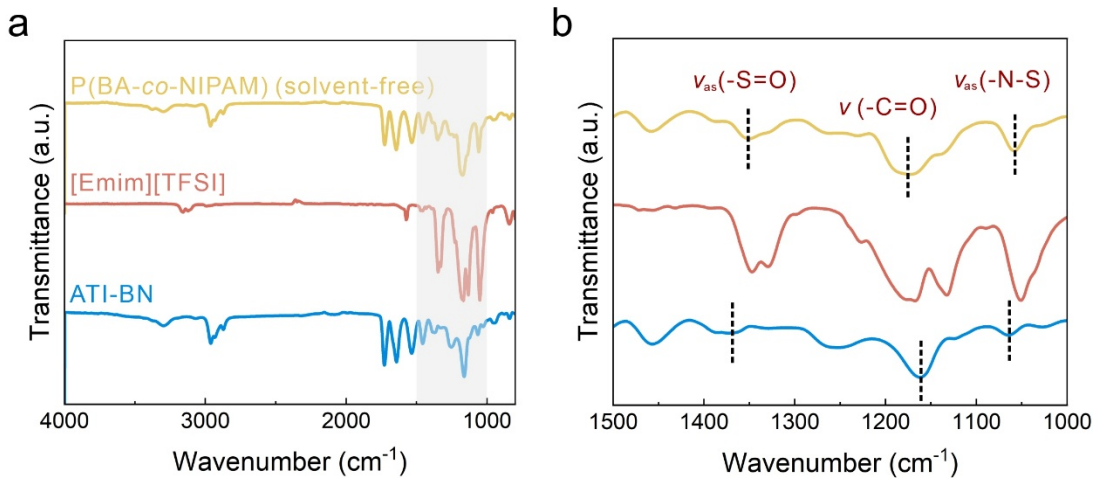

143

144 **Supplementary Figure 8. FTIR spectra of solvent-free P (BA-co-NIPAM), solvent**
145 **[Emim] [TFSI], and ionogel ATI-BN.** a) Wavenumbers in the range of 800-4000 cm^{-1}.
146 b) Wavenumbers in the range of 1000-1500 cm^{-1}. The same color refers to the same
147 component.

148

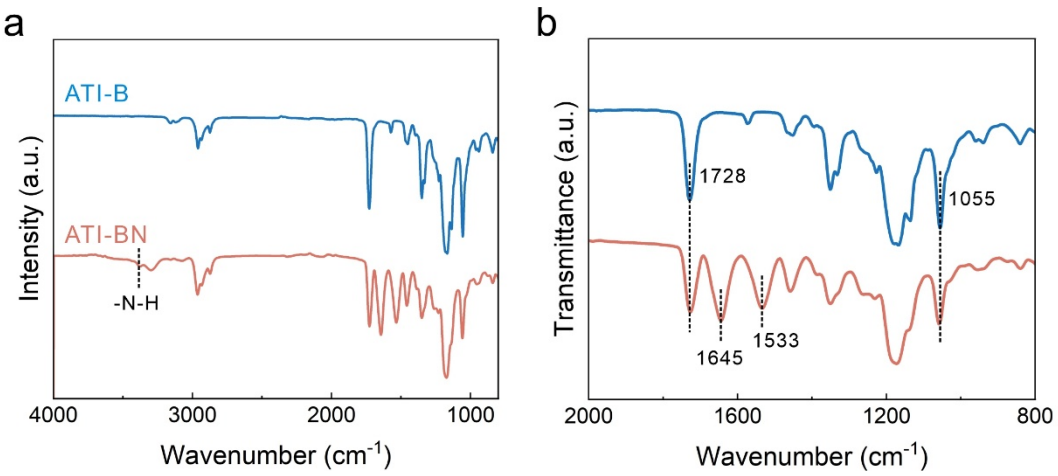

149

150 **Supplementary Figure 9. FTIR spectra of ATI-B and ATI-BN.** a) Wavenumbers in
151 the range of 800-4000 cm^{-1}. b) Wavenumbers in the range of 800-2000 cm^{-1}. The same
152 color refers to the same component.

153

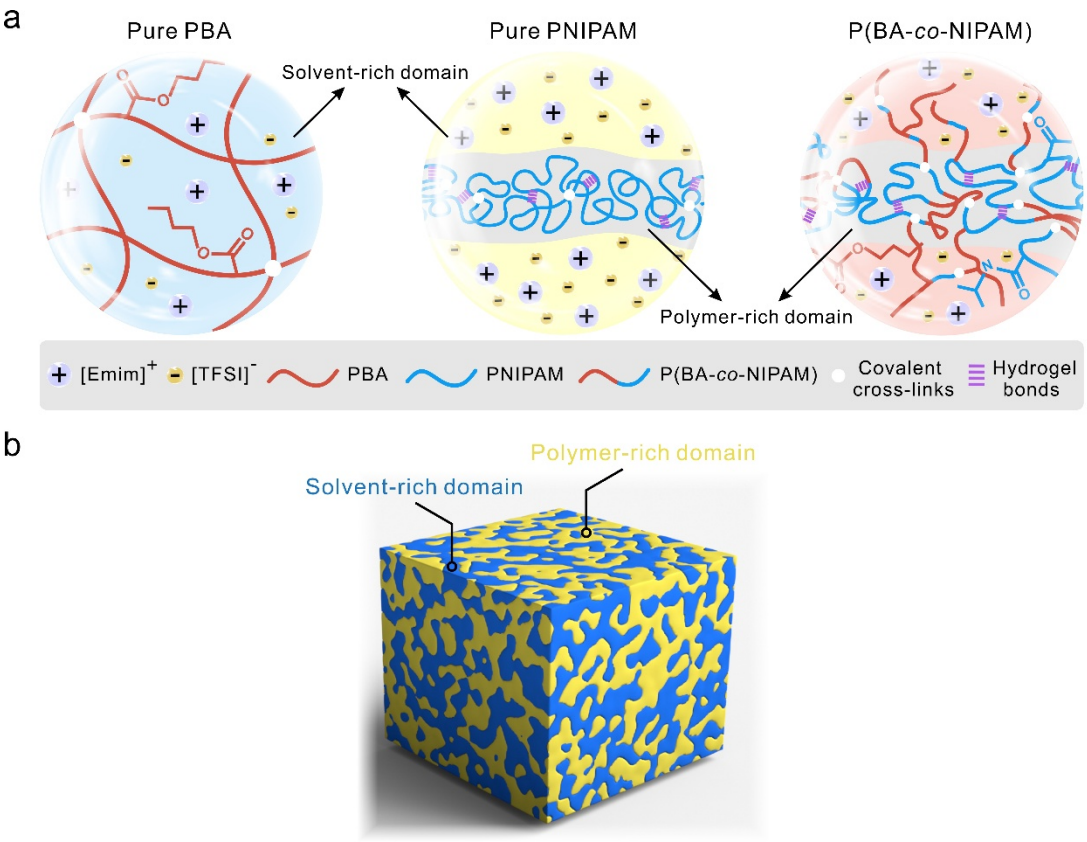

154

155 **Supplementary Figure 10. Schematic of phase separation in ATI-BN.** a)
156 Homopolymer networks of PBA and PNIPAM; and copolymer networks of P(BA-co-
157 NIPAM) in phase-separated structures. b) Bicontinuous networks in in situ phase-
158 separated structures.

159

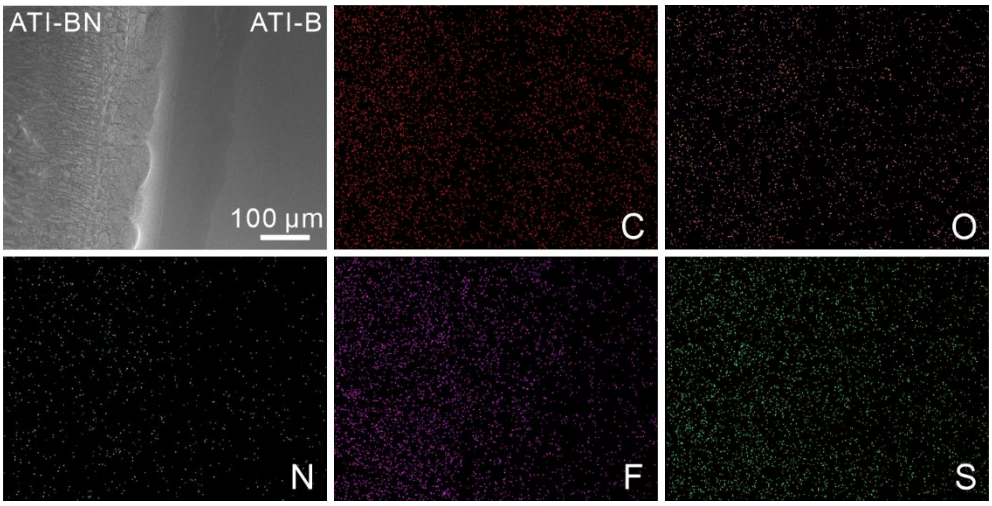

Supplementary Figure 11. Cross-section SEM image and EDS mapping of ATI.

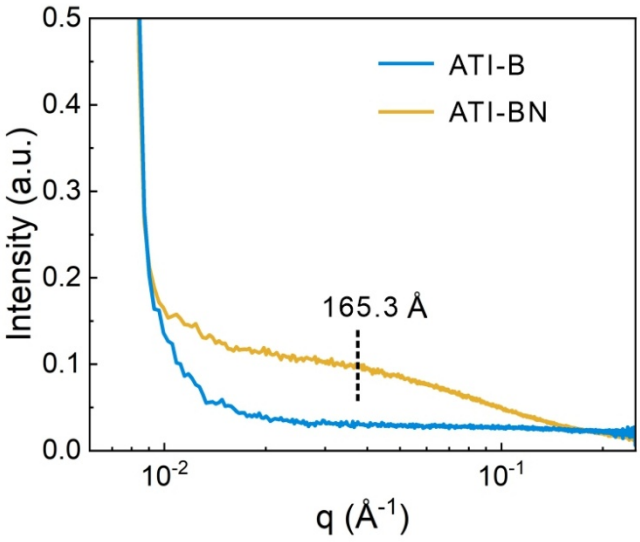

163

164 **Supplementary Figure 12. 1D SAXS spectra of ATI-BN.**

165

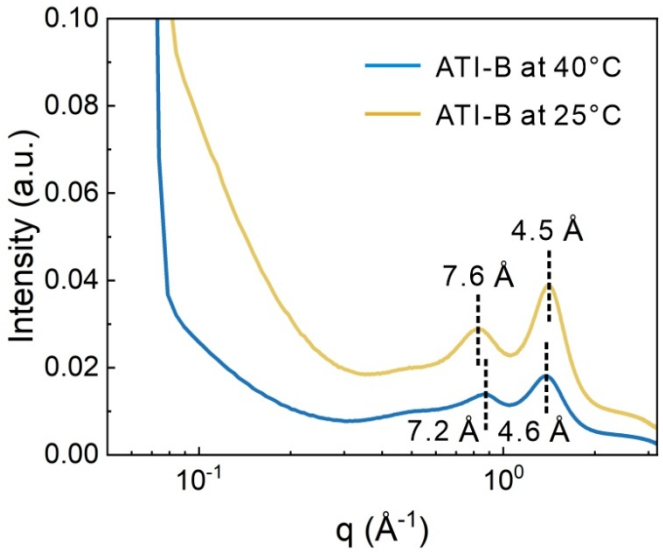

166

167 **Supplementary Figure 13. 1D WAXS spectra of ATI-B.**

168

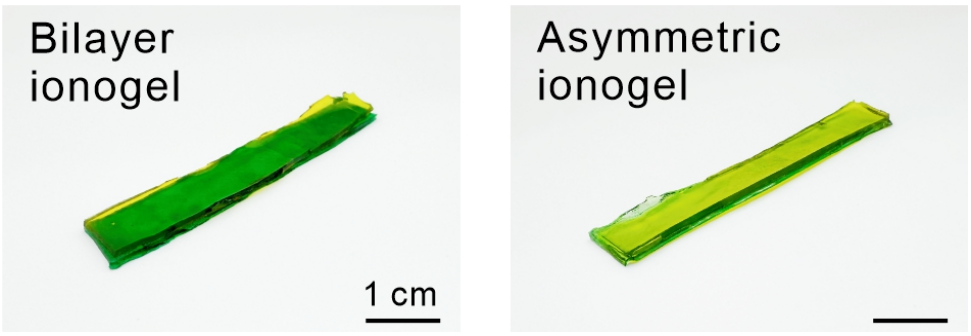

Supplementary Figure 14. Optical photographs of bilayer ionogel and asymmetric ionogel after staining treatment.

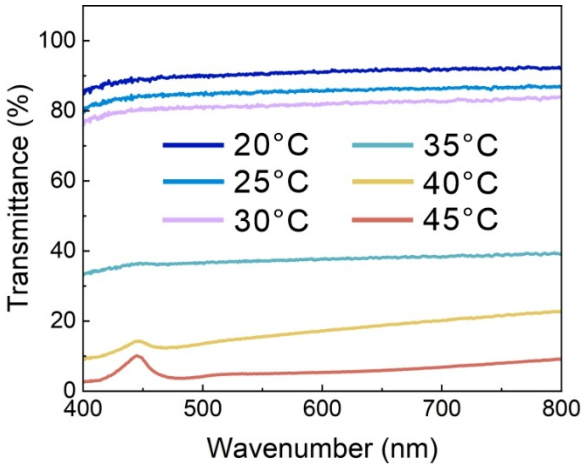

Supplementary Figure 15. The transmittance of ATI within the visible light range at temperatures between 20-45℃.

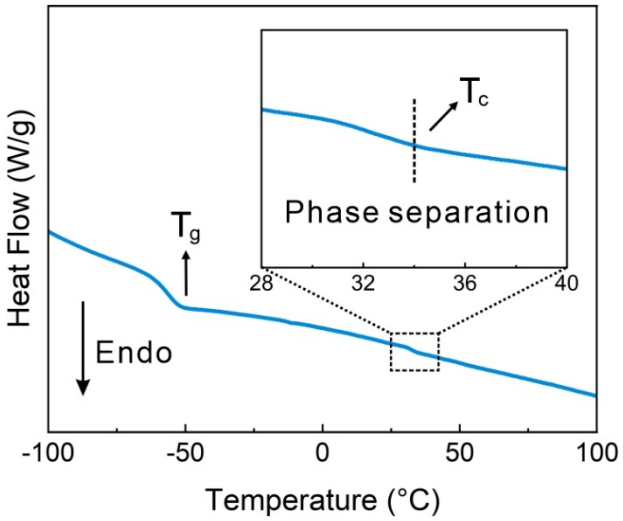

Supplementary Figure 16. DSC curve of ATI-B in the temperature range of -100 to 100°C.

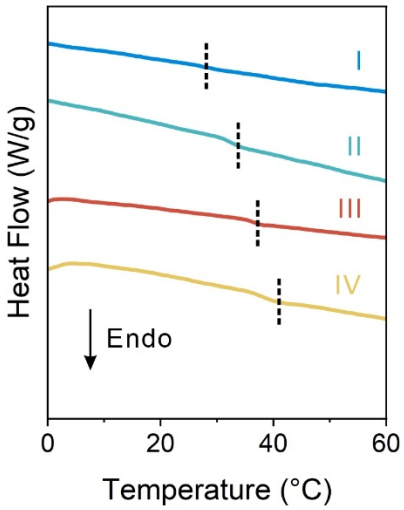

Supplementary Figure 17. DSC curves of ATI-B in different polymer/IL ratios.

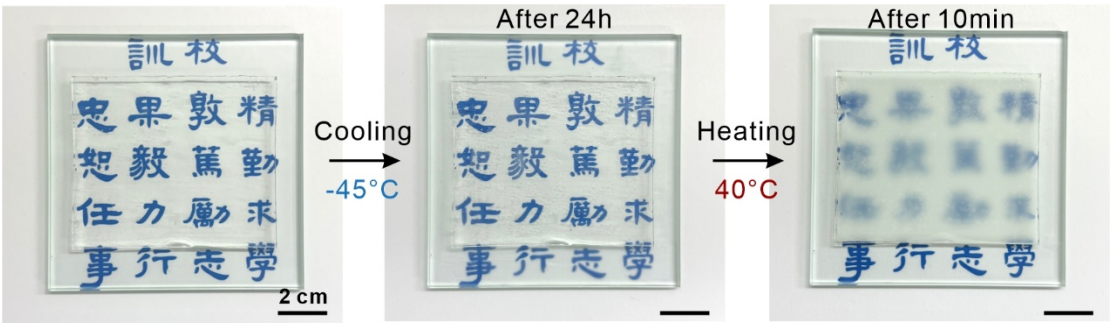

Supplementary Figure 18. Transparency changes of ATI-BN during freezing-heating process (the motto of XJTU in the background, used with permission).

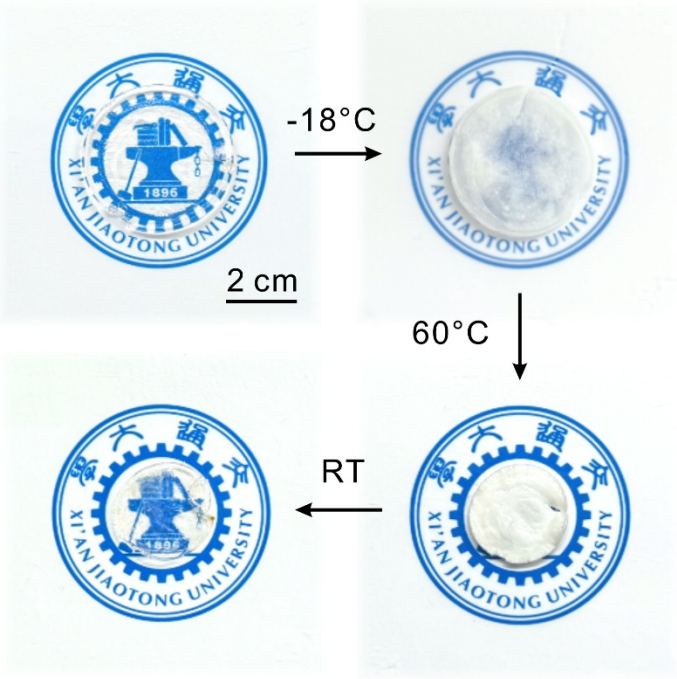

Supplementary Figure 19. Morphological changes in PNIPAM hydrogels during freezing-heating process (the XJTU school emblem in the background, used with permission).

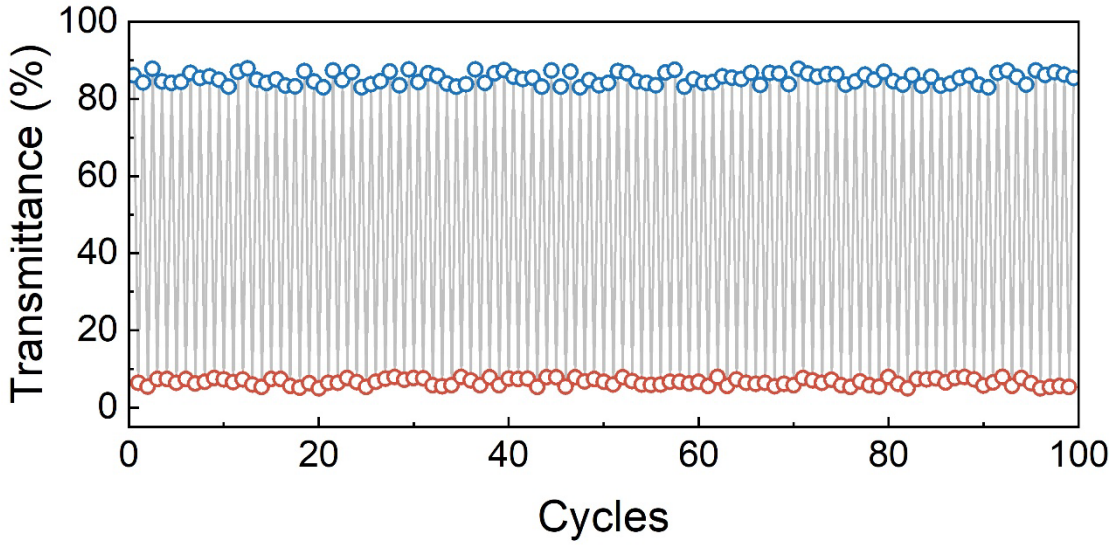

193

194 **Supplementary Figure 20. Changes in transmittance (at 550 nm wavelength) of**
195 **ATI over 100 cycles of freezing and heating from −45°C to 40°C.**

196

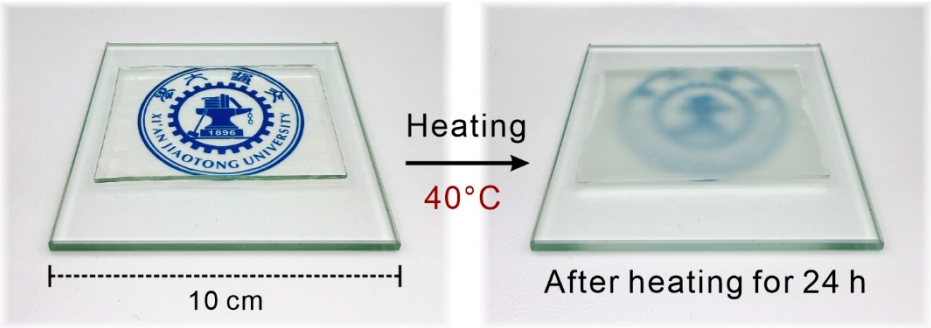

Supplementary Figure 21. Optical photographs of ATI before and after 24h continuous heating (the XJTU school emblem in the background, used with permission).

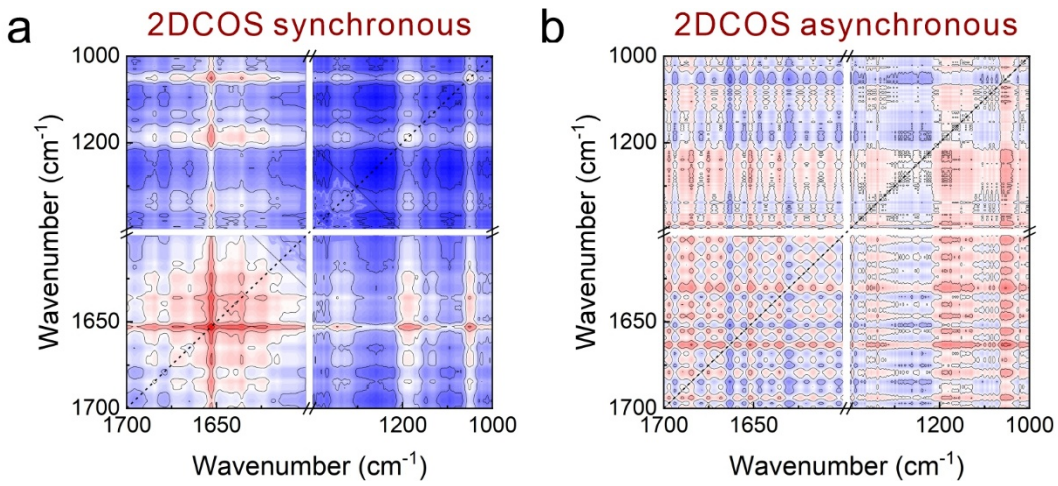

202

203 **Supplementary Figure 22. 2D correlation spectra of temperature-dependent FTIR**
204 **of ATI.** a) 2DCOS synchronous spectra and b) 2DCOS asynchronous spectra. In
205 2DCOS spectra, the warm colors (red) represent positive intensities, while cold colors
206 (blue) represent negative ones.

207

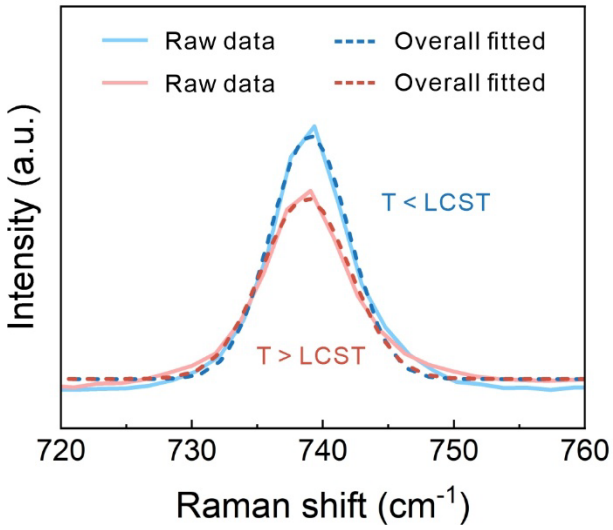

208

209 **Supplementary Figure 23. Temperature-dependent Raman spectra above and**
210 **below LCST, including fitted and raw data.**

211

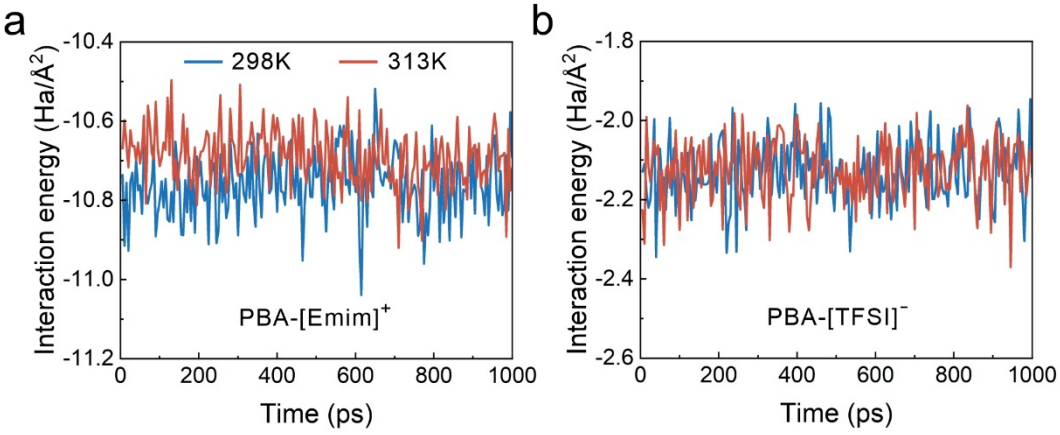

212

213 **Supplementary Figure 24. Interaction energy variations per unit area in the MD**
214 **simulation system.** a) PBA-$[Emim]^+$ interaction energy and b) PBA-$[TFSI]^-$
215 interaction energy.

216

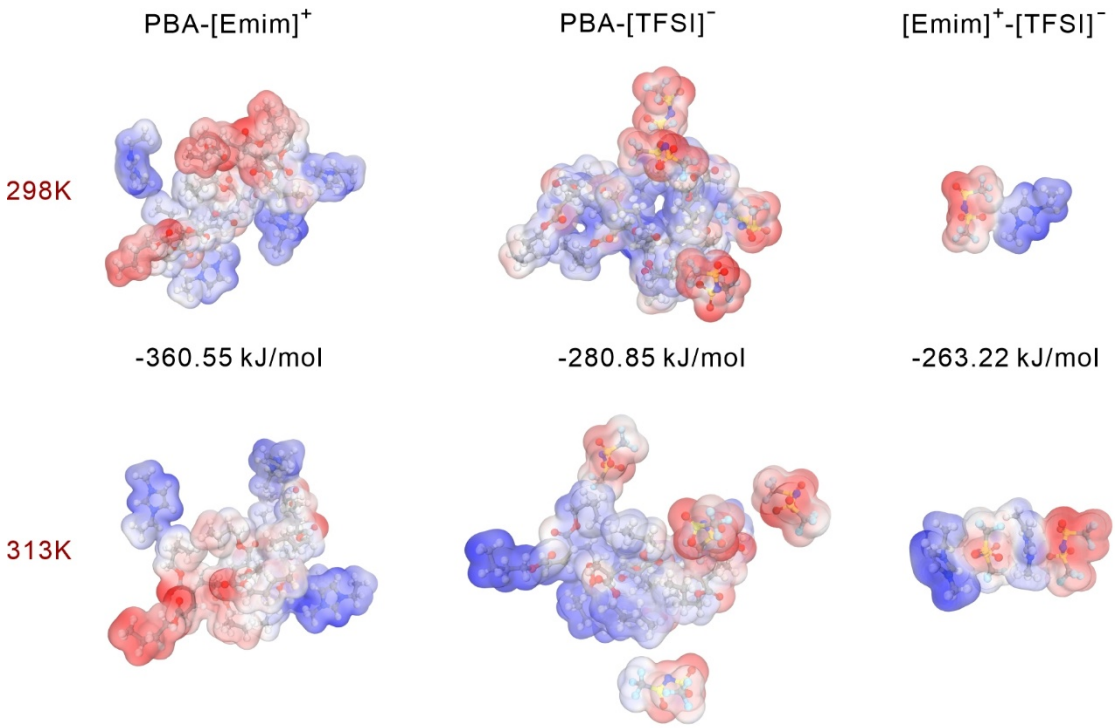

Supplementary Figure 25. Optimized molecular configurations and ESP simulations of the three main interactions at different temperatures in MD simulations.

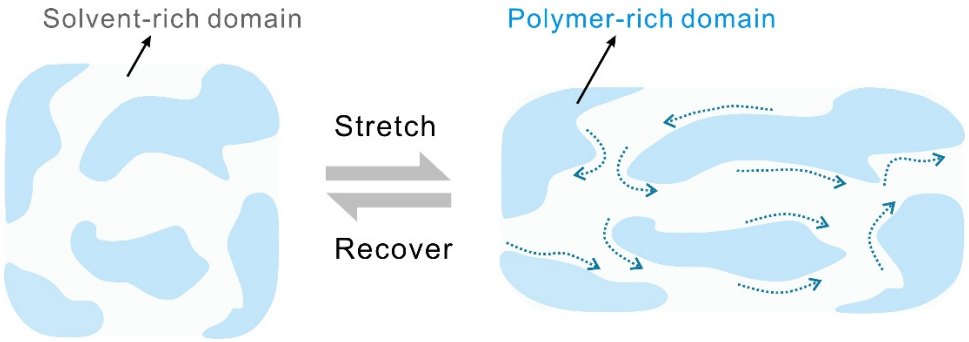

Supplementary Figure 26. Schematic of interphase load-transfer and energy-dissipation pathway in a phase-separated structure.

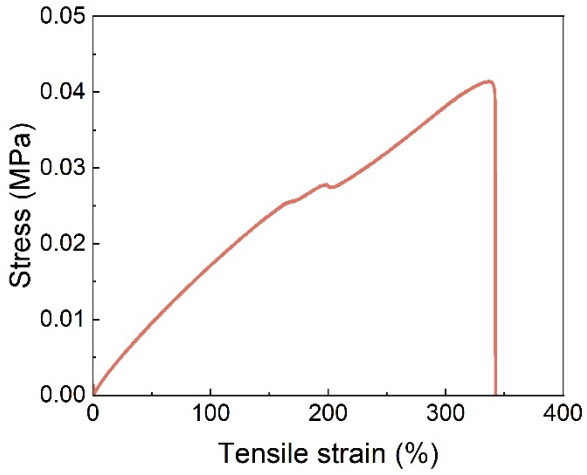

226

227 **Supplementary Figure 27. Stress-strain curves of pure PBA ionogel.**

228

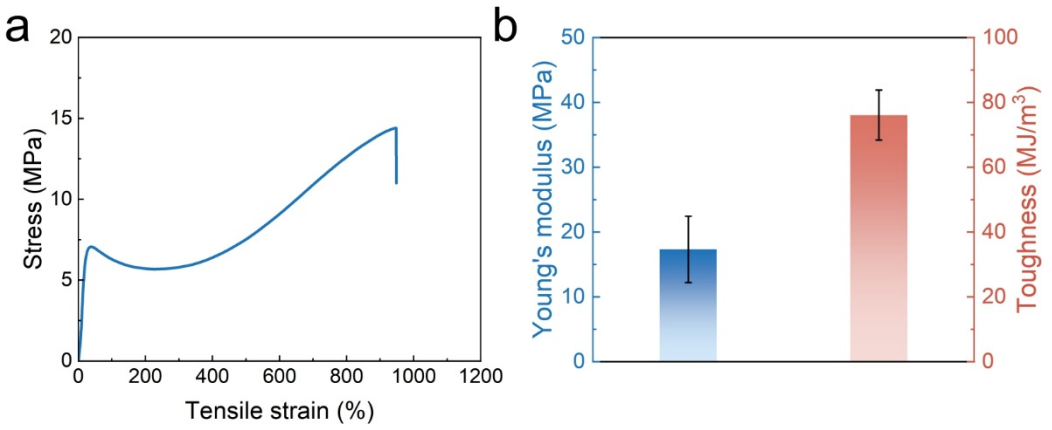

229

230 **Supplementary Figure 28. Mechanical properties of pure P(BA-*co*-NIPAM)**
231 **ionogel. a) Stress-strain curve. b) Young's modulus and toughness.**

232

Supplementary Figure 29. Demonstration of weak mechanical properties of PNIPAM hydrogels.

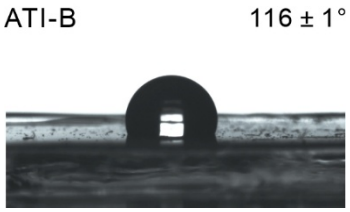

Supplementary Figure 30. Water contact angle image of ATI-B.

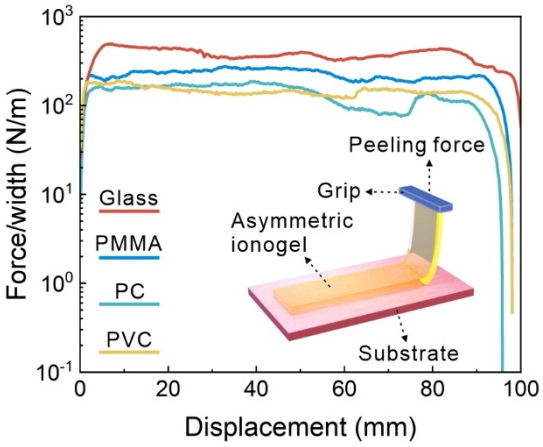

240

241 **Supplementary Figure 31. The 90° peel strength of ATI on different substrates,**

242 **with the insets showing the schematic of the testing method.**

243

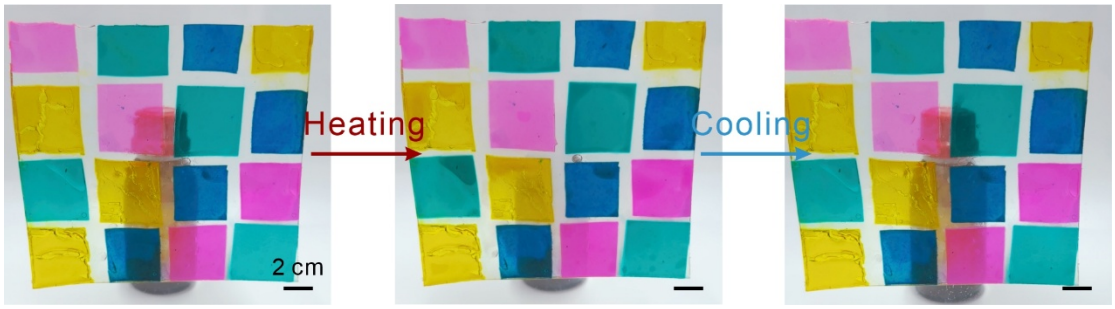

Supplementary Figure 32. Demonstration of transparency change during heating-cooling process of ATI after modular staining.

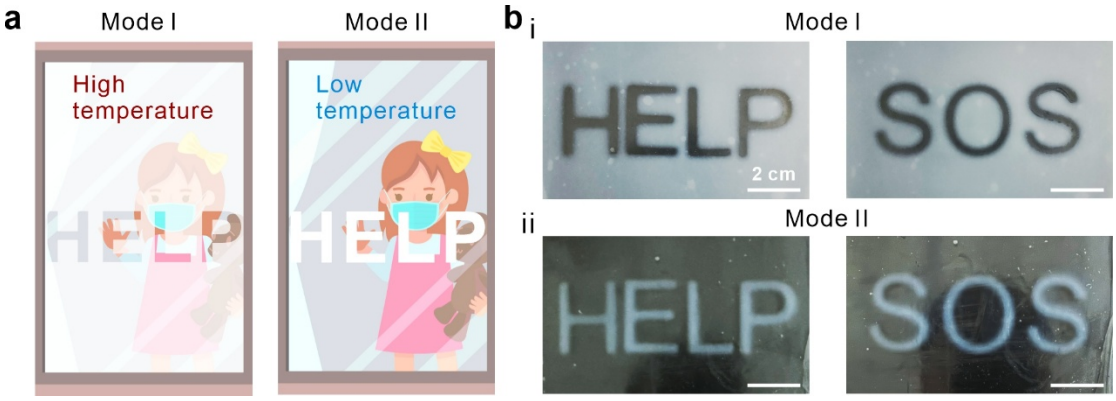

Supplementary Figure 33. Schematic diagram of information display using ATI-based smart display windows. a) Schematic for application in high and low temperature environments. b) Demonstration of application effects, including i) in high temperature environments (using cold objects as stamps) and ii) in low temperature environments (using hot objects as stamps).

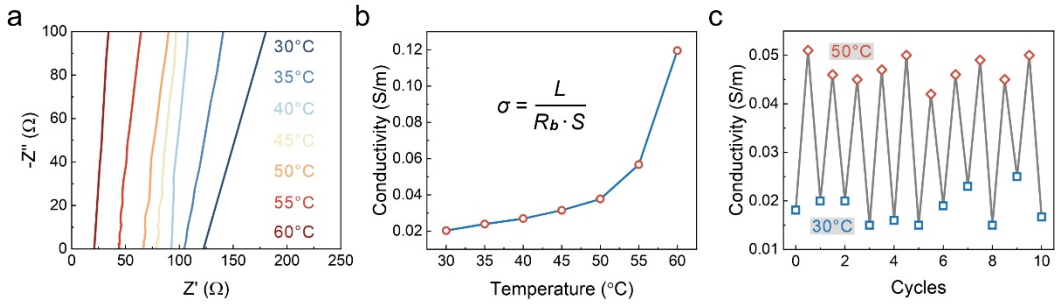

255

256 **Supplementary Figure 34. Electrical conductivity test results.** a) EIS curve. b)
257 Curve of electrical conductivity versus temperature. c) Stability of electrical
258 conductivity during heating-cooling cycles.

259

Supplementary Table 1. Formulations of ATI-B with different LCSTs.

Group	Additions (Monomers in mmol)				LCST (℃)
	BA	[Emim][TFSI]	1173	EGDMA	
I	19.5	6.4	0.05 mol%	0.05 mol%	28
II	23.4	5.1			34
III	27.3	3.8			38
IV	31.2	2.5			41

Supplementary Table 2. Multiplication results of the signs of each cross-peak in 2DCOS synchronous and asynchronous spectra (Supplementary Figure 22) of the ATI-B.

1050	−	−	−	
1346	−	−		
1180	−			
1650				
	1650	1180	1346	1050

According to Noda's rule, the final specific order for ATI-B during heating is given as follows (→ means prior to or earlier than): ν_{as}(-N-S) ($[TFSI]^-$, 1050 cm^{-1}) → ν_{as}(-S=O) ($[TFSI]^-$, 1180 cm^{-1}) → ν_s(-S=O) ($[TFSI]^-$, 1346 cm^{-1}) → ν_{as}(-C=N) (imidazole ring of $[Emim]^+$, 1650 cm^{-1}).

Supplementary Table 3. Temperature-dependent T_{sol} and T_{lum} properties of ATI.

Temperature	T_{sol}	T_{lum}
20℃	75.7%	86.4%
45℃	18.9%	8.1%
Δ	56.8%	78.3%

Supplementary Note 1. FTIR analysis of ATIs.

With the introduction of PBA, the characteristic peaks in [Emim][TFSI] located at 1050 and 1347 cm^{-1} attributed to -N-S antisymmetric telescoping vibration and -S=O antisymmetric telescoping vibration, respectively, move to 1055 and 1351 cm^{-1}. Moreover, the characteristic peaks of -C-H symmetric stretching vibration and antisymmetric stretching vibration attributed to methyl group in PBA shift from 2873 and 2958 cm^{-1} to 2875 and 2960 cm^{-1}, respectively. All the blue shifts of the above characteristic peaks prove that strong ion-dipole interactions form between IL and the polymer (Fig. 2b)[6]. Similarly in ATI-BN, the formation of strong ion-dipole phase interactions is evidenced by the blue shifts of the characteristic peaks in the ionogel at 1058 and 1350 cm^{-1} attributed to the -N-S antisymmetric telescoping vibration and the -S=O antisymmetric telescoping vibration, as compared to the solvent-free P(BA-co-NIPAM). It is noteworthy that the occurrence of the red shift of the -C=O characteristic peak at 1175 cm^{-1} attributed to the ester group in the BA chain segment could be attributed to the increase in the bond length due to the steric effect in the phase-separated structure (Supplementary Fig. 8)[7].

Supplementary Note 2. Two-dimensional correlation spectroscopy (2DCOS).

Two-dimensional correlation spectroscopy (2DCOS) is an analytical technique originally proposed by Noda[8, 9]. It facilitates the interpretation of spectroscopic intensity variations induced by various external perturbations, including time, temperature, concentration, pressure, and electric field strength[10, 11]. By spreading spectral peaks over two dimensions, 2Dcos resolves spectral overlap and enhances spectral resolution.

A 2D correlation map is characterized by two independent wavenumber axes (ν_1, ν_2) and a correlation intensity axis. Analyses typically yield two types of spectra: synchronous and asynchronous. The correlation intensities in these maps reflect whether spectral changes occur in-phase (synchronous) or out-of-phase (asynchronous) relative to each other.

Synchronous Spectrum: This spectrum represents simultaneous or coincidental intensity changes at wavenumbers ν_1 and ν_2 in response to the external perturbation. The synchronous spectrum is symmetric across its diagonal. Peaks appearing on the diagonal are termed autopeaks. Their intensity is always positive, representing the autocorrelation magnitude of perturbation-induced molecular vibrations at each specific wavenumber. Significant autopeaks indicate regions where spectral intensity changes prominently under perturbation. Peaks appearing off the diagonal are termed cross-peaks. They can be either positive or negative. A positive cross-peak indicates that the intensity changes at ν_1 and ν_2 occur in the same direction (both increase or both decrease) during the perturbation. Conversely, a negative cross-peak signifies that the intensity changes at ν_1 and ν_2 occur in opposite directions (one increases while the other decreases).

Asynchronous Spectrum: This spectrum depicts sequential or temporally unsynchronized intensity changes at ν_1 and ν_2. Unlike the synchronous spectrum, the asynchronous spectrum is asymmetric with respect to its diagonal and contains only off-diagonal cross-peaks, which can be positive or negative. Asynchronous cross-peaks develop exclusively when the dynamic intensity variations at ν_1 and ν_2 are out of phase

(e.g., one delayed or accelerated relative to the other). Crucially, these peaks appear only if ν_1 and ν_2 arise from different molecular sources or functional groups experiencing distinct effects due to the perturbation. Thus, asynchronous cross-peaks are particularly powerful for resolving overlapped bands originating from different chemical species, phases, or functional groups within dissimilar molecular environments.

Supplementary Note 3. Entropy-driven dynamic phase separation in ATI-B.

Numerous studies report that hydrogen bonding and cation-π interactions can induce ordered structures between ILs and polymers, thereby generating a negative mixing entropy (ΔS_{mix}). Similarly, we propose that oriented solvation driven by ion-dipole interactions in our system could serve as the driving force for the observed lower critical solution temperature (LCST) phase behavior. At room temperature, the Gibbs free energy of mixing ($\Delta G_{mix} = \Delta H_{mix} - T\Delta S_{mix}$) is negative. However, heating endothermically disrupts these ion-dipole interactions, making ΔH_{mix} less negative. Concurrently, the system gains entropy, increasing the magnitude of the entropic contribution ($T|\Delta S_{mix}|$). When $T|\Delta S_{mix}|$ exceeds $|\Delta H_{mix}|$, ΔG_{mix} becomes positive. This results in entropy-driven phase separation, where the ILs segregate into discrete domains.

Supplementary Note 4. Calculation of transmittance and modulation capability.

The T_{lum} and T_{sol} are calculated by the following equation[12]:

$$T_{lum,sol} = \frac{\int \varphi_{lum,sol}(\lambda)T(\lambda)d(\lambda)}{\int \varphi_{lum,sol}(\lambda)d(\lambda)} \quad (4)$$

where, the φ_{lum} is the luminous vision spectral photo efficiency of the human eye (380-780 nm), φ_{sol} is AM 1.5 standard solar irradiation spectrum (300-2500 nm), $T(\lambda)$ is the spectral transmittance. Where φ_{lum} uses the CIE spectral luminous efficiency for photopic vision covering 380-780 nm and φ_{sol} uses the ASTM G173-03 standard spectrum covering 300-2500 nm.

The ΔT_{lum} and ΔT_{sol} are calculated by the following equation:

$$\Delta T_{lum,sol} = \Delta T_{lum,sol}(Transparent) - \Delta T_{lum,sol}(Opaque) \quad (5)$$

References

S1. Grimme S, Antony J, Ehrlich S, Krieg H. A consistent and accurate ab initio parametrization of density functional dispersion correction (DFT-D) for the 94 elements H-Pu. *The Journal of Chemical Physics* **132**, (2010).

S2. Perdew JP, Ernzerhof M, Burke K. Rationale for mixing exact exchange with density functional approximations. *The Journal of Chemical Physics* **105**, 9982-9985 (1996).

S3. Perdew JP, Burke K, Ernzerhof M. Generalized Gradient Approximation Made Simple. *Physical Review Letters* **77**, 3865-3868 (1996).

S4. Zhang P*, et al.* Biomimetic Superhydrophobic Triboelectric Surface Prepared by Interfacial Self-Assembly for Water Harvesting. *Advanced Functional Materials* **35**, 2413201 (2025).

S5. Dupré A, Dupré P. *Théorie mécanique de la chaleur*. Paris : Gauthier-Villars (1869).

S6. Huang H, Sun L, Zhang Y, Zhang R, Chen C, Sun W. Ionogels Reinforced by Ionophobic Coordination. *Advanced Materials* **n/a**, 2506563.

S7. Yin J*, et al.* Theoretical insights into CO2/N2 selectivity of the porous ionic liquids constructed by ion-dipole interactions. *Journal of Molecular Liquids* **344**, 117676 (2021).

S8. Noda I. Two-dimensional infrared spectroscopy. *Journal of the American Chemical Society* **111**, 8116-8118 (1989).

S9. Noda I. Generalized Two-Dimensional Correlation Method Applicable to Infrared, Raman, and Other Types of Spectroscopy. *Appl Spectrosc* **47**, 1329-1336 (1993).

S10. Sun S-t, Wu P-y. Spectral insights into microdynamics of thermoresponsive polymers from the perspective of two-dimensional correlation spectroscopy. *Chinese Journal of Polymer Science* **35**, 700-712 (2017).

S11. Noda I. Recent advancement in the field of two-dimensional correlation

spectroscopy. *Journal of Molecular Structure* **883-884**, 2-26 (2008).

S12. Li B, Xu F, Guan T, Li Y, Sun J. Self-Adhesive Self-Healing Thermochromic Ionogels for Smart Windows with Excellent Environmental and Mechanical Stability, Solar Modulation, and Antifogging Capabilities. *Advanced Materials* **35**, 2211456 (2023).